Preparation and Analysis of Large, Flat Crystals of Ca^{2+}-ATPase for Electron Crystallography

Dan Shi, Hsiang-Hsin Hsiung, Ron C. Pace, and David L. Stokes
Department of Molecular Physiology and Biological Physics, University of Virginia Health Sciences Center,
Charlottesville, Virginia 22908 USA

ABSTRACT   Obtaining large, flat, well ordered crystals represents the key to structure determination by electron crystallography. Multilamellar crystals of Ca^{2+}-ATPase are a good candidate for this methodology, and we have optimized methods of crystallization and of preparation for cryoelectron microscopy. In particular, high concentrations of glycerol were found to prevent nucleation and to reduce stacking; thus, by seeding solutions containing 40% glycerol, we obtained thin crystals that were 5–30 μm in diameter and 2–10 unit cells thick. We found that removing vesicles and minimizing concentrations of divalent cations were critical to preparing flat crystals in the frozen-hydrated state. Finally, we developed two methods for determining the number of lamellae composing individual crystals, information that is required for structure determination of this crystal form. The first method, using low magnification images of freeze-dried crystals, is more practical in our case. Nevertheless, the alternative method, involving analysis of Laue zones from electron diffraction patterns of slightly tilted crystals, may be of general use in structure determination from thin, three-dimensional crystals.

INTRODUCTION

The calcium pump (Ca^{2+}-ATPase) from sarcoplasmic reticulum (SR) plays a dominant role in muscle relaxation by reducing intracellular calcium concentrations after muscle contraction. Furthermore, Ca^{2+}-ATPase is one of the best studied members of the P-type family of ion pumps, which also includes Na$^+$/K$^+$-ATPase and Ca^{2+}-ATPase from the plasma membrane, the gastric H$^+$/K$^+$-ATPase, and H$^+$-ATPase from yeast. Membership to this family is based not only on homologies in the amino acid sequence, but also on similarities in the transport mechanism (Pederson and Carafoli, 1987): e.g., a common catalytic cycle that includes formation of a covalent phosphoenzyme and inhibition of catalysis by vanadate. Presumably, all members of this family share a common structure and use conformational changes to couple the hydrolysis of ATP to ion transport, even though the individual pumps transport a wide variety of ions with various stoichiometries (Green, 1992). Recently, there has been much effort directed toward determining the transmembrane topology of these pumps. As a result, there is substantial evidence for both 8 and 10 transmembrane crossings, although direct structural studies have been at a resolution too low to resolve this question (Stokes et al., 1994).

Structural studies have advanced somewhat further for Ca^{2+}-ATPase than for other members of this family. For example, a large number of spectroscopic studies have measured distances between probes on various chemically defined sites on the Ca^{2+}-ATPase molecule (Bigelow and Inesi,

1992). Ongoing x-ray diffraction studies of partially oriented pellets of SR have determined the mass distribution across the membrane (Herbette et al., 1985), have documented changes in this distribution upon phosphorylation (Blasie et al., 1985), and most recently have located sites for lanthanides before and after phosphorylation (Asturias et al., 1994). In addition, three different crystal forms have been discovered (Dux and Martonosi, 1983; Dux et al., 1985, 1987) and have lead to several three-dimensional reconstructions by electron microscopy. So far, these three-dimensional reconstructions have come from a two-dimensional crystal form within the native SR membrane; in the case of rabbit muscle SR (Taylor et al., 1986), crystallization is induced by vanadate and, in the case of scallop SR (Castellani et al., 1985), crystals form spontaneously in rigor conditions. Initial reconstructions from negatively stained crystals defined the overall shape of the molecule at rather low resolution (25–30 Å) and its disposition in the membrane. A more recent reconstruction from frozen-hydrated, unstained specimens revealed the structure of the transmembrane domain (Toyoshima et al., 1993) and allowed a first attempt at fitting helices into the slightly higher resolution (14 Å) envelope (Stokes et al., 1994). A more detailed model for the calcium-binding site (Inesi, 1994; Inesi et al., 1994) was constructed by juxtaposing transmembrane helices that contained the six residues previously implicated in calcium binding by site-directed mutagenesis (Clark et al., 1989). As would be expected for Ca^{2+}-ATPase, this model provides sites for cooperative binding of two calcium ions in addition to a narrow access for these ions to the cytoplasmic side of the membrane.

These kinds of details of transmembrane structure, as well as the physical locations of chemical labeling sites, must be determined ultimately by direct structural determination at higher resolution. Such studies may be possible with a different crystal form of Ca^{2+}-ATPase (Dux et al., 1987). The

---

corresponding crystals are formed from detergent-solubilized, purified Ca^{2+}-ATPase (Pikula et al., 1988) and are composed of a limited stack of membranous lamellae (Taylor et al., 1988; Stokes and Green, 1990b). These crystals are well ordered, as indicated by electron diffraction at ~4 Å resolution from untilted crystals in the frozen-hydrated state; thus, a projection map was determined at 6-Å resolution by combining this electron diffraction with phase data from images (Stokes and Green, 1990a). However, these original crystals were rather small (1–2 μm in diameter) and tended to clump together, thus preventing them from lying flat on the specimen support. A larger size would be desirable, and flatness is absolutely essential for collecting data from tilted crystals, which could then be used for three-dimensional reconstruction of this crystal form. Indeed, attempts have been made to increase crystal size and to make them unilamellar by manipulating concentrations of glycerol, polyethylene glycol, salts, and temperature (Misra et al., 1991; Varga et al., 1991). In both studies, crystal stacking was reduced and crystal size increased somewhat but, unfortunately, unilamellar crystals could not be reproducibly obtained. In the current work, we have developed a crystallization procedure that produces significantly larger crystals and a method for making them flat. In addition, we have developed methods for determining their thickness, which will be required for structure determination.

MATERIALS AND METHODS

Preparation and crystallization of Ca^{2+}-ATPase

SR vesicles from rabbit hind leg white muscle were prepared by the method of Eletr and Inesi (1972). The final protein concentration was adjusted to ~20 mg/ml and stored at −80°C. Ca^{2+}-ATPase was purified from SR vesicles by Reactive Red affinity chromatography, as originally described by Coll and Murphy (1984) and later modified by Stokes and Green (1990b). The fractions were assayed for ATPase activity by the coupled enzyme method (Warren et al., 1974) in the presence of 2.5 mg/ml octaethylene glycol dodecylether (C$_{12}$E$_8$, Nikko Chemical Co., Tokyo, Japan) and for protein concentration by the Lowry method (Lowry et al., 1951). The peak fractions were pooled to give a protein concentration of 3–4 mg/ml and an ATPase activity of 8–10 μmol/min/mg at 25°C; based on Coomasie blue staining of polyacrylamide gradient gels, Ca^{2+}-ATPase represented >98% of the resulting protein.

Ca^{2+}-ATPase was crystallized by the method described by Stokes and Green (1990b). Briefly, the concentrations of purified Ca^{2+}-ATPase and C$_{12}$E$_8$ were adjusted to 2 and 1.7 mg/ml, respectively. Then various concentrations of lipid (egg yolk phosphatidyl choline, Avanti Polar Lipids, Alabaster, AL) were added to achieve weight ratios between 0.6:1 and 1.2:1 (lipid-to-detergent). The solutions were sealed in microdialysis cells holding either 20 or 50 μl, and the cells were dialyzed against a solution containing 100 mM KCl, 10 mM CaCl$_2$, 3 mM MgCl$_2$, 20 mM MES pH 6.0, 5 mM dithiothreitol (DTT), 2 μg/ml butylated hydroxytoluene, 1 mM NaN$_3$, 0.1 mg/ml C$_{12}$E$_8$, and 20 or 40% glycerol for 1 day to 6 weeks. Normally, crystallization is carried out at 4°C, but for the current work we also tried −20 and 25°C. To prevent the solutions from freezing at the lower temperature, the concentration of glycerol was first increased to 40% by adding it either to dialysis buffer or directly to the crystal solutions.

Electron microscopy

Crystals were negatively stained by adding 3 successive drops of 1% uranyl acetate to crystals that had adsorbed to carbon-coated grids (Stokes and

Green 1990a). For frozen-hydrated samples, a small volume of crystal solution was dialyzed against a buffer containing 100 mM KCl, 20 mM MES pH 6.0, 0.5 mM CaCl$_2$, and 3 mM DTT and then centrifuged for ~40 min at low speed (~180 rpm) to separate crystals from small vesicles; the pellet was then resuspended in this same dialysis buffer. The absence of glycerol tends to provide thinner, more uniform layers of ice after freezing, and low concentrations of divalent cations seem to promote adsorption of crystals to the carbon film. In some cases, crystals were centrifuged onto the carbon film to encourage maximal adsorption. To do this, grids covered with a holey carbon film were placed in a custom-made adaptor (shaped roughly like a wine glass with a well ~3 mm in diameter by ~2 mm high). Crystal solution (~15 μl) was added, and the assembly was centrifuged at 800–1200 rpm for ~40 min. After removing the grids, the holey carbon film was blotted
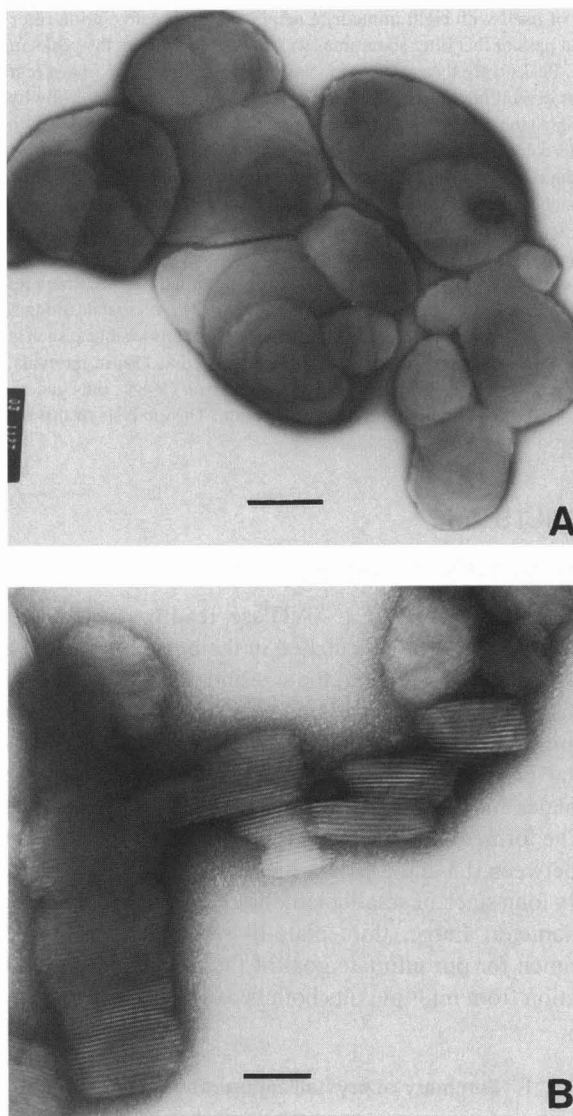

FIGURE 1 Two different crystal morphologies are observed depending primarily on the lipid-to-detergent ratio during crystallization. (A) Thin, plate-like crystals grow at high ratios and provide a view along the c axis. (B) Long cylindrical crystals grow at lower lipid-to-detergent ratios and provide a range of views perpendicular to the c axis (e.g., along the a or the b axes). The plate-like morphology is preferable for electron crystallography because the corresponding crystals are much larger and thinner than the long cylindrical crystals. Scale bars represent 1 and 0.2 μm in A and B, respectively.

from the side opposite to the adsorbed crystals, thus drawing the solution through the holes, and plunged into an ethane slush (Toyoshima, 1989). Electron diffraction was recorded in a Philips 400T electron microscope using a cryoholder (Gatan Inc., Warrendale, PA) operating at its minimum temperature ($-174°C$). The radiation dose used for each electron diffraction pattern was ~0.5–1 electron/Å^2.

Thickness determination

Two different methods were explored for determining the thickness of individual crystals. For the first, a high contrast, low magnification image of each crystal was recorded from the defocused, unscattered beam in diffraction mode. The images were digitized at 50-μm intervals; then individual crystals were masked, and a histogram of image density was created. The peaks in these histograms often were blurred by random noise inherited from the low dose images; therefore, each pixel was replaced with the average of itself with eight immediate neighbors (3×3 convolution filter). A second pass of this filter sometimes was needed to sharpen the peaks maximally. Peaks were then assigned to particular features in the image (carbon film or crystalline layers). This assignment could be verified easily by assigning a single color to all density around a given peak, thus generating a pseudo-color image that clearly showed the distribution of densities within the image. As described in Results, this method was much more successful if crystals were first freeze-dried by heating the specimen holder to $-100°C$ for at least 30 min while in the electron microscope.

For the second method, frozen-hydrated crystals were tilted very slightly (2–5°) and electron diffraction patterns were recorded with a camera length of 1600 mm. Given the spacing of these Ca^{2+}-ATPase crystals along the c direction (~185 Å), one expects Laue zones to be easily visible at such small tilt angles. Such diffraction patterns were digitized at 15-μm intervals and processed as described by Baldwin and Henderson (1984), thus generating a list of h, k, and amplitude for each reflection. The analysis of this data is described in Results and in Fig. 4.

RESULTS

Dependencies of crystallization

Detergent-solubilized Ca^{2+}-ATPase readily crystallizes in space group C2 when incubated in the presence of lipid and calcium at pH 6. However, the size and shape of the resulting crystals vary greatly, depending primarily on the precise ratio of lipid to detergent (Stokes and Green, 1990b). Two main crystal morphologies are dominant: those resembling thin, flat plates and those resembling long, cylindrical worms (Fig. 1). The former is composed of a short stack of lamellae ranging between 0.5 and 3 μm in diameter, whereas the latter is a very long stack of smaller lamellae between 0.1 and 0.5 μm in diameter. Large, thin, plate-like crystals are the ideal specimen for our ultimate goal of three-dimensional reconstruction from multiple tilts both because they lay flat on the

specimen support and because they are thin enough to be penetrated easily by the electron beam.

These crystals are generally grown by dialysis against a standard solution containing 20% glycerol at 4°C for several days to weeks. Distinct trends in crystal morphology were noted previously (Stokes and Green, 1990b) as the lipid-to-detergent ratio was systematically varied. We were able to reproduce these results and, while doing so, have noted the time required to achieve the various crystal morphologies. These observations (Table 1) can be summarized succinctly, as follows: at low lipid-to-detergent ratios, many cylindrical crystals grow very quickly, whereas at high lipid-to-detergent ratios, only vesicles are observed; at the interface between these two conditions, a small number of large crystals grow very slowly. Because both the size and the growth rate depended on the lipid-to-detergent ratio, we hypothesized that this ratio somehow was controlling the rate of nucleation. According to this hypothesis, when nucleation is rapid, one would expect a large number of small crystals, and when nucleation is slow, one would expect a small number of crystals that have a chance to grow very large. In the case of our Ca^{2+}-ATPase crystals, this growth occurs predominantly in the plane of the lamellae, generating thin plates with a large diameter; extensive stacking is observed only in conditions that favor nucleation, thus generating the long cylindrical crystals. Clearly, control of nucleation represents the key to growing large, thin crystals, and we undertook, therefore, further studies to manipulate the parameters of nucleation and growth.

Formation of large, plate-like crystals

To control the nucleation, we first tried using 40% glycerol and low temperature ($-20°C$) during crystallization. The effects of these two factors on Ca^{2+}-ATPase crystallization have been studied previously by Varga et al. (1991). Unlike these authors, however, we found that no crystals were formed in the presence of 40% glycerol after several weeks of incubation either at 4°C or at $-20°C$. Assuming that nucleation was somehow inhibited by elevated concentrations of glycerol, we reasoned that large crystals might be obtained by initiating nucleation in a buffer containing 20% glycerol and then promoting pure growth by transferring crystals to one containing 40% glycerol. Indeed, this "seeding" strategy proved highly successful, generating thin, coherent crystals with a diameter of 5–30 μm after 4–10

TABLE 1 Summary of crystallization results

Incubation time (d)	Lipid-to-detergent ratio by weight						
	0.6	0.7	0.8	0.9	1.0	1.1	1.2
1	ccc	p + v	vv	vvv	—	—	—
2–7	ccc	pp*	p	p + v	vv	vvv	vvv
14–28	ccc	pp*	pp	p	p + v	p + v	vv

c = cylindrical crystals; p = plate-like crystals; v = vesicles. The number of characters corresponds to the relative abundance (e.g., vvv = lots of vesicles and p = few plate-like crystals).
*These platelike crystals were somewhat smaller (0.5 μm) than others, suggesting a transition between cylindrical crystals and plate-like crystals.

weeks of incubation. Surprisingly, these giant crystals formed irrespective of the lipid-to-detergent ratio or of the temperature of incubation in the buffer with 40% glycerol, although crystal growth was much slower at −20°C. The

only requirement seemed to be that crystals exist in the solution before transfer (i.e., no de novo crystallization in 40% glycerol).

Because the giant crystals took many weeks to grow, we were able to examine them at intermediate stages and thus to elucidate the steps in their formation. Soon after transfer from the buffer with 20% glycerol to that with 40% glycerol, crystal size increased. However, upon closer inspection, these larger crystals consisted of multiple domains, suggesting that they were the direct result of fusion between many smaller crystals (Fig. 2 A). At this stage, these crystals were useless for data collection because each domain diffracted independently. Eventually, these domains realigned themselves and fused such that, after 4–10 weeks, crystals with a single, coherent domain were obtained (Fig. 2 B). The final size of these crystals was independent of the lipid-to-detergent ratio during crystallization. However, within a given batch of crystals, the smaller crystals (5–10 μm in diameter) were usually thinner (2–5 layers thick) and were therefore best for collection of electron diffraction.

In addition to this rational approach to growing large crystals by control of nucleation, we also obtained large crystals by rapid (less than 7 d) growth at 25°C in a buffer containing 20% glycerol. Even though they grew quickly, all crystals were large (5–10 μm) regardless of the lipid-to-detergent ratio. However, crystals grown at low ratios adopted a distinct diamond shape (Fig. 2 C) with very straight edges and well defined angles, as one might expect from large, three-dimensional crystals. Their size was 3–5 μm × 6–10 μm and, although they were relatively thin at first, they got progressively thicker with increased incubation time.

Electron diffraction of large, plate-like crystals

The formation of giant crystals with a single, coherent crystalline domain has two great advantages for collection of three-dimensional data at high resolution: (1) The number of molecules contributing to the diffraction pattern is 2- to 20-fold larger than crystals grown by previous methods (Stokes and Green, 1990a; Misra et al., 1991; Varga et al., 1991), which should produce an increase in the signal-to-noise ratio in electron diffraction by 4- to 400-fold; (2) the grouping or aggregation of the smaller crystals can be controlled, thus allowing crystals to lie flat on the carbon support (compare Fig. 1 A with Fig. 2, B and C). To capitalize on these advantages, the innate order of crystals and their flatness must be optimized. The degree of order was assessed by electron diffraction from untilted crystals, which we found to be quite
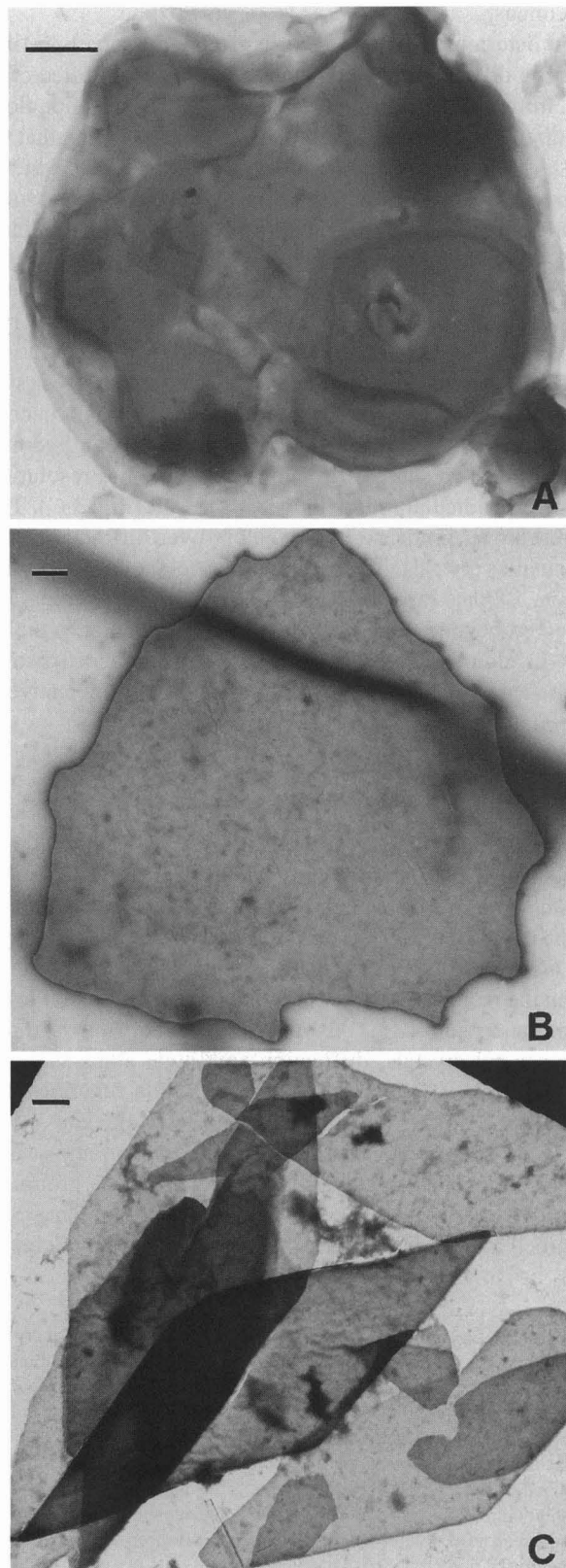
FIGURE 2 Low magnification images of large, plate-like crystals. (A) Soon after inducing fusion of smaller crystals with 40% glycerol, multiple domains were apparent within some sort of limiting envelope; these multidomain crystals produced no useful diffraction. (B) After several weeks of incubation, the individual domains coalesced to form a single, coherent domain that yields excellent electron diffraction (see Fig. 3). (C) Crystals grown at room temperature adopted a distinctive diamond shape with well defined edges and angles. All scale bars represent 1 μm.
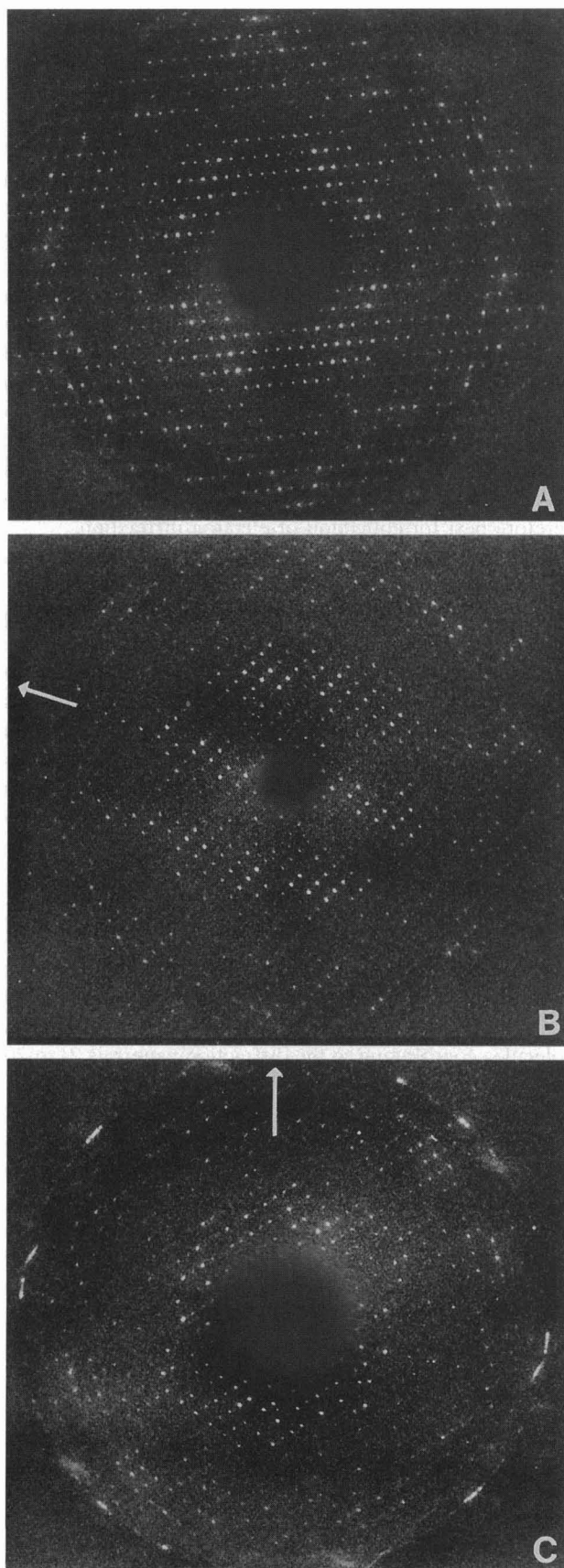
strong to ~3.6-Å resolution, both for crystals grown by fusion (Fig. 3 A) and for diamond-shaped crystals grown at room temperature (not shown). The signal-to-noise ratio from the larger crystals within a given batch (>20-μm diameter and >5 layers thick) was somewhat lower, perhaps due to an increase in inelastic scattering from these thicker specimens.

To determine the flatness of crystals on the carbon film, electron diffraction patterns were recorded from tilted crystals. Initially, these diffraction patterns were very poor along the direction perpendicular to the tilt axis, indicating that the crystals were not flat. Therefore, we investigated ways to make the crystals flat and eventually found two factors that improved this situation. Thus, the best diffraction patterns were obtained by removing excess vesicles from the crystal solution and by lowering the concentration of divalent cations to an absolute minimum. Gentle centrifugation of crystals onto the carbon support before freezing sometimes was used and was effective in increasing the number of crystals adsorbed to the grid, but no significant improvement in crystal flatness was achieved. Thus, prepared, frozen-hydrated crystals yielded sharp diffraction spots to ~4-Å resolution, even perpendicular to the tilt axis, at 45° tilt (Fig. 3 C). This represents an immense improvement over diffraction from the smaller crystals grown by previous methods (Stokes and Green, 1990a; Varga et al., 1991), from which nothing was observed beyond ~15-Å resolution perpendicular to the tilt axis. In addition, crystals at very small tilts produced distinct Laue zones (Fig. 3 B, see below), which is also indicative of very flat crystals.

Measuring crystal thickness

To merge data from individual crystals into a three-dimensional data set, we must determine the thickness of crystals in terms of the number of unit cells along the c axis of the crystal. This is because, unlike two-dimensional crystals (Amos et al., 1982), the diffraction amplitude is sampled along the reciprocal lattice lines that run perpendicular to the membrane plane (Z^*). Also, unlike infinitely thick, three-dimensional crystals, diffraction amplitude along this axis (c^* in our case) is not infinitely sharp delta functions, but spread by a function that depends on crystal thickness (Fig. 4). Thus, once we know the thickness, we can adjust data from individual images to allow merging with a group.

In our first method for determining crystal thickness, we recorded images from the unscattered electrons by defocus-

FIGURE 3   Electron diffraction patterns from the large, plate-like crystals indicate that they are quite well ordered and flat. (A) An untilted crystal generates the expected mm symmetry of the (h,k,0) projection. (B) A slightly tilted crystal (~3°) generates Laue zones as the tilted plane in Fourier space cuts through successive reflections along c^*. (C) Sharp, isotropic diffraction from a crystal at 45° tilt extends to high resolution in all directions, indicating that it is very flat. The edge of the patterns correspond to a resolution of 3.5 Å; the arrows in b and c indicate the tilt axis. The very strong, broad reflections at high resolution in c are from crystalline ice (frost) on the crystal and are at 3.7-Å resolution.

ing the unscattered beam in diffraction mode (Fig. 5, A and C). Density steps corresponding to overlapped crystals were used to determine the thickness of individual crystals. To aid in the visualization of these steps, a histogram of image density was constructed (Fig. 5, B and D), which contains peaks corresponding to the densities within the particular layers; the magnitude of each peak reflects the total area in the image covered by the relevant thickness. To determine the absolute thickness corresponding to an individual peak, we subtracted the density associated with the film fog (e.g., over a grid bar) and determined the absorbance associated with each crystalline layer. Assuming that the film responded linearly over the density range used, the absorbance of a given crystal (A) is defined as $\log(D_c/D)$, where D_c is the corrected film density of the carbon support; the absorbance should then be proportional to crystals thickness (Lamvik and Davilla,

1989). This method worked well for freeze-dried crystals (Fig. 5, C and D; Table 2), and the number of unit cells composing individual crystals could be deduced easily (~0.1 natural log absorbance units per crystal layer according to the last two columns in Table 2). However, this relationship was not maintained for frozen-hydrated crystals (Fig. 5, A and B; Table 3), apparently because the ice was thicker over the crystals than over the carbon film. Nevertheless, the crystal overlap provides a constraint with which this additional ice thickness can be determined. Assuming there is the same amount of ice over all of the crystals, the area marked "3" (Fig. 5 A) corresponds to one crystal + ice, and the area marked "6" corresponds to two crystals + ice, then $2 \cdot A_3 - A_6$ gives the absorbance corresponding to this extra ice (0.5 natural log absorbance units in this particular example). Taking this extra ice thickness into account, the absorbances from the frozen-hydrated crystals do follow the expected linear dependence on thickness (last two columns in Table 3).

We also have investigated an alternative method for determining crystal thickness using electron diffraction of slightly tilted crystals. For untilted crystals, the corresponding diffraction data lie in a plane through the three-dimensional Fourier transform satisfying the condition that $l = 0$, i.e., all reflections of the type $(h, k, 0)$. For tilted crystals, this plane is inclined at the corresponding angle through Fourier space such that reflections at successive values of l are sampled as one moves normal to the tilt axis; reflections along the tilt axis remain in the original, untilted plane. This gives rise to Laue zones seen in Fig. 3 B as strips of reflec-
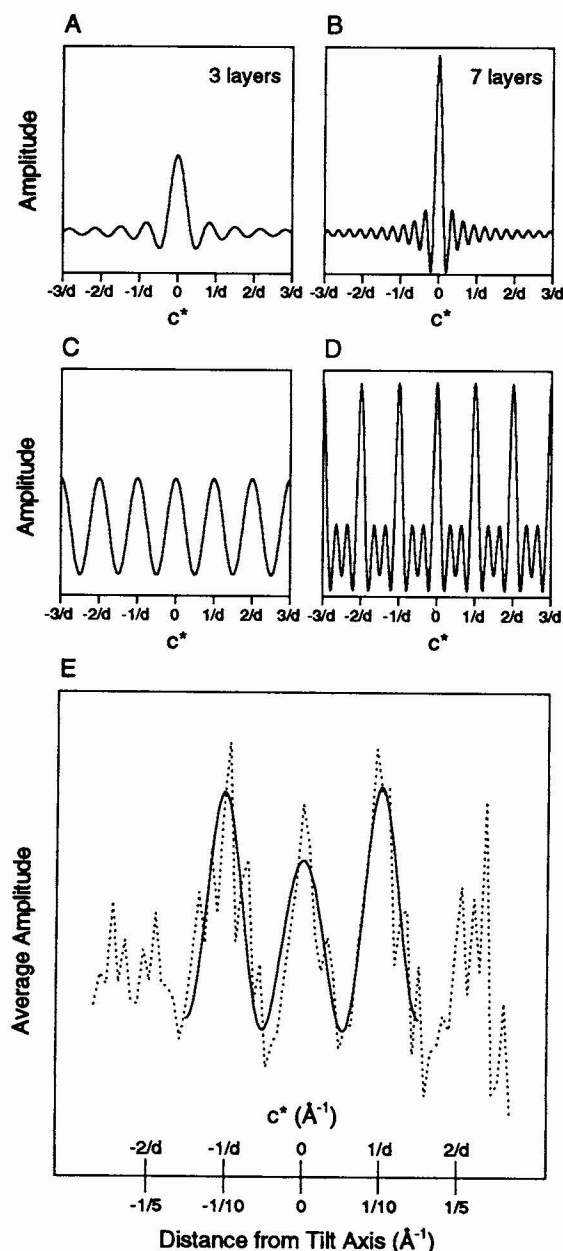

FIGURE 4 Reflections from thin, three-dimensional crystals are not infinitely sharp, but are spread out along the c^* axis in reciprocal space. A and B represent the Fourier transforms of two boxes of different width, corresponding to crystals with a thickness of 3 or 7 unit cells. Because the crystals are thinnest along the c axis, the abscissa represents the reciprocal coordinate along c^*; d represents the repeat distance along this c axis in real space. In general, a crystal containing n unit cells can be represented by a box of width $n \cdot d$, and the Fourier transform of this box would be $\sin(\pi c^* nd)/\pi c^*$. The first zero in this function occurs when $c^* = 1/nd$, and its maximum height (at $c^* = 0$) is $n \cdot d$. The crystals are effectively of infinite thickness along a and b axes because they have many thousand unit cells along these directions and the reflections, therefore, are not spread out along either the a^* or b^* directions. C and D represent the sum of functions at intervals of $1/d$ that one would expect from a crystal with a unit cell spacing of d, i.e., reflections are expected at intervals of $1/d$ and each reflection is convoluted with the transform of the box function. Note that the few reflections shown have been assumed to have equal amplitude for this model. E represents the electron diffraction pattern in Fig. 3 B that has been fitted with the expected transform of the box. The amplitudes of reflections have been grouped depending on their distance from the tilt axis, and the average amplitudes ($\cdots\cdots$) have been fitted by least-squares to a sum of three functions at regular intervals (——). The amplitude of each function was variable and ultimately corresponds to the structure factor for the corresponding reflection. The lower set of numbers along the abscissa represent the distance of reflections from the tilt axis in Fig. 3 B. Because the spacing of the first maximum is by definition at a spacing of $1/d$, the values along the abscissa can be converted into the coordinate along the c^* axis, represented by the upper values along the abscissa. The fit is consistent with a crystal thickness of three unit cells and, assuming a unit cell spacing along c of 185 Å, with a tilt angle of 3°.

FIGURE 5 Thickness determination from low magnification images. The images were recorded from the defocused, unscattered beam in diffraction mode of frozen-hydrated (A) or freeze-dried (C) crystals. A fraction of the image containing the relevant features was masked, and a histogram of image density was calculated (B and D). The peaks in the histogram correspond to various thicknesses of the specimen. This correspondence is indicated by the labels: "c" to carbon, "g" to the grid bar, and numbers to crystalline layers (see Tables 2 and 3). In C, the crystal marked "2" was not included in the area used for the histogram in D.
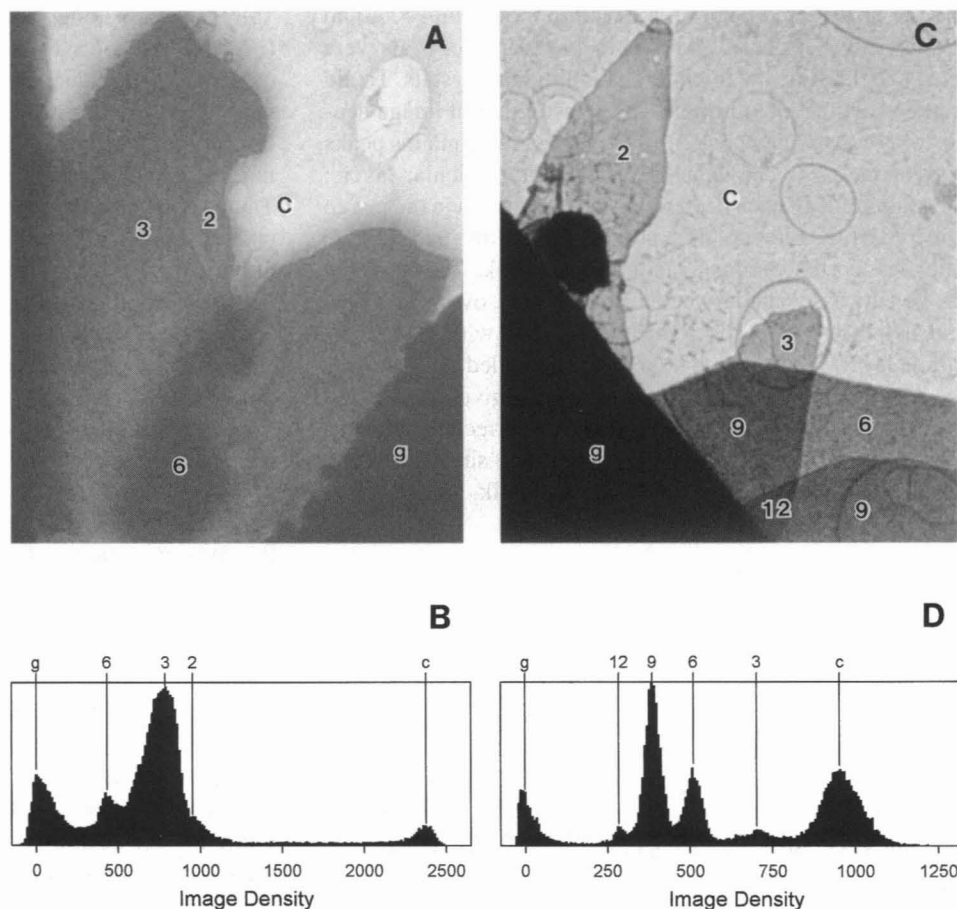
TABLE 2 Thickness of freeze-dried crystals in Fig. 5C

	Density* relative to film fog (D)	ln(D)	A[‡]	Deduced number of unit cells[§]
c[¶]	954	6.86	0	0
2	788	6.67	.19	2
3	707	6.56	0.3	3
6	508	6.23	0.63	6
9	385	5.95	0.91	9
12	281	5.64	1.22	12
g	0			

*Density taken from histogram in Fig. 5D with value for film fog (peak g) subtracted. Values in this column referred to as D in subsequent columns; D_c refers to the density for the carbon film (denoted "c"). D_2 is not present in the histogram because the image area used for the histogram did not include this crystal. The corresponding image was recorded at 400 kV.

[‡]Absorbance of each feature relative to the carbon film defined as $\ln(D_c/D)$. Thus, $A_3 = \ln(D_c/D_3)$ and corresponds to the absorbance over the crystal marked "3".

[§]If $A_1 = 0.1$, where A_1 corresponds to the absorbance of a single unit cell, then the expected linear relationship between absorbance and crystal thickness is upheld.

[¶]This column identifies the feature on the image and the peak in the histogram shown in Fig. 5 D; thus, "c" corresponds to the carbon film, "g" corresponds to the film fog measured over the grid bar, and numbers correspond to individual crystalline layers.

TABLE 3 Thickness of frozen-hydrated crystals in Fig. 5A

	Density* relative to film fog (D)	ln(D)	A[‡]	$A - A_{ice}$[§]	Deduced number of unit cells[¶]
c[‖]	2362	7.77	0		0
2	966	6.87	0.9	0.4	2
3	795	6.68	1.09	0.59	3
6	440	6.09	1.68	1.18	6
g	0				

*Density taken from histogram in Fig. 5 B with value for film fog (peak g) subtracted. Values in this column referred to as D in subsequent columns; D_c refers to the density for the carbon film (denoted "c"). The corresponding image was recorded at 120 kV.

[‡]Absorbance of each feature relative to the carbon film defined as $\ln(D_c/D)$. Thus, $A_3 = \ln(D_c/D_3)$ and corresponds to the absorbance over the crystal marked "3".

[§]A_{ice} is the absorbance due to the additional ice over the crystals. This has been deduced to be 0.5 by evaluating the expression $2 \cdot A_3 - A_6$ (see text).

[¶]If $A_1 = 0.2$, where A_1 corresponds to the absorbance of a single unit cell, then the expected linear relationship between absorbance and crystal thickness is upheld.

[‖]This column identifies the feature on the image and the peak in the histogram shown in Fig. 5 B; "c" corresponds to the carbon film, "g" corresponds to the film fog measured over the grid bar, and "2," "3," and "6" correspond to crystalline layers.

tions running parallel to the tilt axis; the strip of reflections intersecting the origin corresponds to $l = 0$, the next strip to either side corresponds to $l = \pm 1$, the next strip to $l = \pm 2$.

If the crystal were infinitely thick, then each strip of reflections would be very narrow. In fact, the observed width of each strip corresponds to the spread in amplitude due to limited crystal thickness. Theoretically, this spread corresponds

to the transform of a box function ($\sin(\pi t c^*)/\pi c^*$, where $t =$ crystal thickness, Fig. 4), and Fig. 4 E shows a least-squares fit of the average amplitude from Fig. 3 B with this function, indicating that this crystal was 3 unit cells thick. The data in Fig. 4 E are derived from unnormalized amplitudes and, therefore, are not compensated for the natural variation in amplitude across the diffraction pattern. A more rigorous treatment would involve normalization of observed amplitudes against a reference data set. This could be done by iteratively merging a large number of diffraction patterns, starting with no reference set and generating an improved reference set after each round of iteration. However, we had a very low success rate in recording Laue zones from slightly tilted crystals (3–5°), and the alternative method using low magnification images of freeze-dried crystals, therefore, is more practical for our purposes.

DISCUSSION

Methods for electron crystallography have improved greatly during the past two decades, primarily because of the pioneering work of Henderson and co-workers on bacteriorhodopsin (Baldwin and Henderson, 1984; Henderson et al., 1986). Ultimately, this work resulted in an atomic model for bacteriorhodopsin (Henderson et al., 1990), and the same methodology has been used subsequently to determine the atomic structures of light harvesting complex (Kühlbrandt et al., 1994) and porin (Jap et al., 1991). Despite these improvements in imaging and computer analyses, the real key to electron crystallography lies in the quality of the crystals and in their preparation for electron microscopy. In particular, the size, order, and flatness of crystals must all be optimal if one hopes to collect data at high resolution. In the case of Ca^{2+}-ATPase crystals, earlier studies showed them to be innately ordered, but relatively small ($\sim$1 μm), and their tendency to aggregate into clumps prevents them from lying flat on the substrate (Stokes and Green, 1990a). Furthermore, the multilamellar nature of Ca^{2+}-ATPase crystals represents a further complication over single-layered specimens, requiring novel strategies in data collection and analysis. Through the current work, we aimed to make the crystals more suitable for data collection at high tilt and to develop a specific strategy for coping with their multilamellar nature.

Crystallization

Observations of crystal growth suggest a direct causality between nucleation and stacking of the lamellae that compose these crystals. Circumstantial evidence for this causality comes from our earlier observations that many small crystals were formed at low lipid-to-detergent ratios (abundant nucleation) and that these small crystals contained many more lamellae than the relatively few, large crystals found at high lipid-to-detergent ratios (sparse nucleation, Stokes and Green, 1990b). If this causality is indeed correct, then any factor affecting nucleation would also be expected to affect stacking in the corresponding way. In the current work, we

observed that 40% glycerol did exactly that; it severely limited the extent of stacking while preventing nucleation altogether. The very large, thin crystals we obtained at room temperature suggest that this elevated temperature also reduces nucleation while limiting the extent of stacking. Although our observations do not suggest a specific mechanism for these effects, they are consistent with the idea that stacking interactions are less stable than interactions within the plane of the lamellae. Accordingly, both high glycerol concentrations and high temperature would act to destabilize the system and preferentially disrupt the weaker interactions that lead to stacking. In the case of glycerol, Gekko and Timasheff (1981a, b) concluded that it was generally excluded from protein surfaces, thus leading to preferential hydration of the protein and enhanced solvent ordering, and perhaps these effects are involved in destabilization of Ca^{2+}-ATPase crystals. A different view was taken by Varga et al. (1991), who proposed that reduced nucleation is a result of the reduced mobility of proteins in the viscous solutions containing 40% glycerol and that stacking may be discouraged by direct binding of glycerol to the protein surface.

In contrast to the inhibitory effects on nucleation and stacking, we found that high concentrations of glycerol induced fusion of small, preformed crystals and encouraged growth within the plane of the lamellae. This in-plane growth was also observed by Varga et al. (1991). It is interesting that glycerol should promote growth in one direction while preventing growth in another. This dichotomy must reflect the nature of the interactions along these two directions: although stacking is mediated by cytoplasmic domains of Ca^{2+}-ATPase, in-plane growth probably involves interactions within the hydrophobic bilayer between detergent, lipid, and transmembrane domains of Ca^{2+}-ATPase. One plausible explanation for fusion and in-plane growth is that glycerol destabilizes the half-micelle of detergent that we presume exists around the perimeter of each lamella. We have hypothesized previously the existence of this ring of detergent to explain both the morphology of the crystals and the dependence of crystal size on the detergent-to-lipid ratio (Stokes and Green, 1990b). According to this hypothesis, this detergent-to-lipid ratio determines the ratio of lamellar circumference (occupied purely by the ring of detergent) to lamellar area (containing lipid and detergent in a fixed proportion). Thus, low detergent-to-lipid ratios generate large diameter lamellae, and high ratios generate small diameter lamellae. If an increase in glycerol concentration were to destabilize this ring of detergent, fusion and in-plane growth of crystals would serve to reduce dramatically the ratio of circumference to area and, thus, to limit the number of detergent molecules involved in this ring. Varga et al. (1991) also pointed out that increased solvent ordering by glycerol (Gekko and Timasheff, 1981a, b) might serve to promote hydrophobic interactions within the lipid/detergent bilayer and thus promote in-plane growth. If this were the case, it may be significant that we have used a pure detergent ($C_{12}E_8$) and lipid headgroup (phosphatidyl choline), whereas other

investigators have used a heterogeneous detergent (BRIJ 36T) and mixed lipids from the SR membrane (Pikula et al., 1988; Misra et al., 1991; Varga et al., 1991), which may provide more poorly defined transitions within the hydrophobic phase.

The technique of fusing small crystals to obtain larger ones is not unique to this work, but has been used previously to increase crystal size both for bacteriorhodopsin (Baldwin and Henderson, 1984) and for light-harvesting complex (Wang and Kühlbrandt, 1991). Although specific methods for fusion vary, some extended period of time always seems to be required after fusion to allow the crystalline lattices to reorient to form large, coherent crystalline domains that could then be used for electron diffraction.

Preparation for electron microscopy

Given that our Ca^{2+}-ATPase crystals are much larger and possibly a bit thinner than previously reported, the next hurdle is to make them flat on the specimen support. This issue has been considered in detail by Glaeser and colleagues for deposition of purple membrane patches (two-dimensional bacteriorhodopsin crystals) onto hydrophobic carbon films (Glaeser et al., 1991; Glaeser, 1992). After suspending membranes in 1% glucose, they appear to partition at the air-water interface and are forced onto the carbon film during water evaporation, thus becoming embedded in a layer of highly concentrated glucose. Although the principles of these studies are relevant to Ca^{2+}-ATPase crystals, the specific methodologies are not, because glucose embedding does not successfully preserve Ca^{2+}-ATPase crystals. Instead, we have prepared frozen-hydrated samples, reasoning that the poor preservation by glucose embedding may be due to collapse of the large extramembranous domain of Ca^{2+}-ATPase during drying, which would lead to disordering of the crystalline lamellae.

For preparation of frozen-hydrated samples, the properties of the carbon film must be manipulated both to encourage crystal adsorption and to provide a layer of ice thin enough to allow electron beam penetration. We have previously studied crystal adsorption to freshly cleaved mica for atomic force microscopy (Lacapere et al., 1992) and concluded that the surface of these Ca^{2+}-ATPase crystals was positively charged. Thus, maximal crystal adsorption to the negatively charged mica surface was achieved by minimizing the concentration of divalent cations and by removing vesicles. In the current work, these same factors were critical in making crystals lie flat on the carbon film. Presumably, excess vesicles become trapped under the crystals, thus providing an irregular surface for adsorption, and the divalent cations reverse a negative surface charge present on the carbon film after glow discharge. For electron microscopy, this glow discharge is generally used to alter the surface properties of the carbon film and the nature of the gas used for discharge has been shown to influence both the charge and the hydrophobicity (Dubochet and Groom, 1982). Like many people, we have used amyl amine to obtain a thin layer of ice and, based

on the effects of divalent cations, we conclude that the glow discharged carbon film carries a negative charge. This conclusion is inconsistent with previous work (Dubochet and Groom, 1982), which found alkyl amines to create a positive surface charge. Finally, it seemed plausible that gentle centrifugation of crystals onto the carbon film would promote crystal adsorption and thereby enhance flatness. Unfortunately, we found the effects on flatness were minimal, although the number of adsorbed crystals was increased greatly. Thus, the take-home message seems to be that methods for obtaining flat specimens must be determined empirically for a given type of crystal, using basic principles and common sense only as a general guide.

Crystal thickness

Electron crystallography so far has been applied successfully only to two-dimensional crystals; that is, crystals constrained to a single layer such as a membrane. The Fourier transform of such specimens consists of a two-dimensional array of lattice lines and a given diffraction pattern or image contains data from a plane through Fourier space, which intersects the origin and is inclined about an axis at an angle corresponding to those at which the crystal was tilted in the microscope (Amos et al., 1982). In the case of an infinitely thick, three-dimensional crystal, the lattice lines become a series of discrete reflections along c^* (perpendicular to the lamellae) to generate a three-dimensional lattice. In the case of our Ca^{2+}-ATPase crystals, the finite thickness spreads the discrete reflections depending on the precise thickness of the crystal (i.e., the number of unit cells; see Fig. 4). If all of the crystals were of uniform thickness, then they could be treated as very thick, two-dimensional crystals; the only practical difference would be a more rapid variation in amplitude along c^*, which would require a larger number of images and diffraction patterns to provide adequate sampling at a given resolution. However, Ca^{2+}-ATPase crystals are not necessarily of equal thickness, and the spread of the reflections, therefore, will vary from one crystal to the next. Our strategy, therefore, is to determine the thickness and, thus, to correct the observed data with the appropriate function to obtain the amplitude corresponding to discrete reflections from an infinitely thick crystal. However, frozen-hydrated crystals were somewhat problematic because of differing ice thickness over the crystals and over the carbon. Given the overlap of two crystals, we were able to determine the contribution from the additional ice thickness over the crystals (Table 3), but crystals are not always overlapping and one cannot necessarily assume uniform layers of ice from one crystal to the next. This difficulty can be overcome by simply removing the ice by freeze-drying crystals in the electron microscope (Table 2). A similar problem was encountered previously in the thickness determination of gp32*I crystals by electron energy loss spectroscopy (Leapman et al., 1993). However, because these crystals were embedded in glucose rather than in ice, freeze-drying was not a viable option. In such a case, our alternative method of determining thickness from the dis-

tribution of amplitude across Laue zones might be useful. This method has the advantage of providing an empirically determined "spread function" that includes lack of flatness together with crystal thickness.

It should be noted that phase data from images will be much less sensitive to crystal thickness because the phases should be relatively constant across the main peak of the reflection. The only significant consideration for images will be whether the crystals comprise an even or an odd number of unit cells. Because the phase origin is forced to the middle of the structure (along c^*) during merging of data into a three-dimensional data set, the phase origin will differ by half a unit cell for the two classes of crystals (even or odd). A phase origin shift of half a unit cell will impose a phase shift of π on every other reflection along c^*, which should be easily detected and corrected when individual images are merged into a three-dimensional data set.

CONCLUSIONS

We have improved significantly the preparation of thin, three-dimensional crystals of Ca²⁺-ATPase and now have large, flat crystals suitable for electron crystallography. In addition, we have developed a strategy for determining crystal thickness after freeze-drying the specimen. Thus, diffraction data can be merged together after correcting for the spread of reflections along the c^* axis. Phase data from images will require a different kind of correction, which will also be aided by knowledge of crystal thickness.

Although these methods have been developed for three-dimensional Ca²⁺-ATPase crystals, there was a recent report of crystals of Na⁺/K⁺-ATPase with apparently identical morphology (Taylor and Varga, 1994) that might be analyzed by similar methods. In fact, multilayered crystals appear occasionally in the literature (e.g., Valpuesta et al., 1994) and generally have been abandoned because of the difficulty in their analysis. It is our hope that the principles and techniques we have presented can be applied to future projects, thus extending the range of crystal structures that can be solved by electron crystallography.

REFERENCES

Amos, L. A., R. Henderson, and P. N. T. Unwin. 1982. Three-dimensional structure determination by electron microscopy of two-dimensional crystals. *Prog. Biophys. Mol. Biol.* 39:183–231.

Asturias, F. J., R. F. Fischetti, and J. K. Blasie. 1994. Changes in the relative occupancy of metal-binding sites in the profile structure of the sarcoplasmic reticulum membrane induced by phosphorylation of the Ca²⁺ ATPase enzyme in the presence of terbium: a time-resolved, resonance x-ray diffraction study. *Biophys. J.* 66:1665–1677.

Baldwin, J., and R. Henderson. 1984. Measurement and evaluation of electron diffraction patterns from two-dimensional crystals. *Ultramicroscopy.* 14:319–336.

Bigelow, D. J., and G. Inesi. 1992. Contributions of chemical derivatization and spectroscopic studies to the characterization of the Ca²⁺ transport ATPase of sarcoplasmic reticulum. *Biochim. Biophys. Acta.* 1113:323–338.

Blasie, J. K., L. G. Herbette, D. Pascolini, V. Skita, D. H. Pierce, and A. Scarpa. 1985. Time-resolved x-ray diffraction studies of the sarcoplasmic reticulum membrane during active transport. *Biophys. J.* 48:9–18.

Castellani, L., P. M. Hardwicke, and P. Vibert. 1985. Dimer ribbons in the three-dimensional structure of sarcoplasmic reticulum. *J. Mol. Biol.* 185: 579–594.

Clark, D. M., T. W. Loo, G. Inesi, and D. H. MacLennan. 1989. Location of high affinity Ca²⁺-binding sites within the predicted transmembrane domain of the sarcoplasmic reticulum Ca²⁺-ATPase. *Nature.* 339:476–478.

Coll, R. J., and A. J. Murphy. 1984. Purification of the CaATPase of sarcoplasmic reticulum by affinity chromatography. *J. Biol. Chem.* 259: 14249–14254.

Dubochet, J., and M. Groom. 1982. The mounting of macromolecules for electron microscopy with particular reference to surface phenomena and the treatment of support films by glow discharge. *In* Advances in Optical and Electron Microscopy, Vol. 8. R. Barer and V. E. Cosslett, editors. Academic Press, London. 107–135.

Dux, L., and A. Martonosi. 1983. Two-dimensional arrays of proteins in sarcoplasmic reticulum and purified Ca²⁺-ATPase vesicles treated with vanadate. *J. Biol. Chem.* 258:2599–2603.

Dux, L., K. A. Taylor, H. P. Ting-Beall, and A. Martonosi. 1985. Crystallization of the Ca²⁺-ATPase of sarcoplasmic reticulum by calcium and lanthanide ions. *J. Biol. Chem.* 260:11730–11743.

Dux, L., S. Pikula, N. Mullner, and A. Martonosi. 1987. Crystallization of Ca²⁺-ATPase in detergent-solubilized sarcoplasmic reticulum. *J. Biol. Chem.* 262:6439–6442.

Eletr, S., and G. Inesi. 1972. Phospholipid orientation in sarcoplasmic reticulum membranes: spin-label ESR and proton NMR studies. *Biochim. Biophys. Acta.* 282:174–179.

Gekko, K., and S. N. Timasheff. 1981a. Mechanism of protein stabilization by glycerol: preferential hydration in glycerol-water mixtures. *Biochemistry.* 20:4667–4676.

Gekko, K., and S. N. Timasheff. 1981b. Thermodynamic and kinetic examination of protein stabilization by glycerol. *Biochemistry.* 20: 4677–4686.

Glaeser, R. M. 1992. Specimen flatness of thin crystalline arrays: influence of the substrate. *Ultramicroscopy.* 46:33–43.

Glaeser, R. M., A. Zilker, M. Radermacher, H. E. Gaub, T. Hartman, and W. Baumeister. 1991. Interfacial energies and surface-tension forces involved in the preparation of thin, flat crystals of biological macromolecules for high-resolution electron microscopy. *J. Microsc.* 161:21–45.

Green, N. M. 1992. Evolutionary relationships within the family of P-type cation pumps. *Ann. N.Y. Acad. Sci.* 671:104–112.

Henderson, R., J. M. Baldwin, K. H. Downing, J. Lepault, and F. Zemlin. 1986. Structure of purple membrane from Halobacterium halobium: recording, measurement and evaluation of electron micrographs at 3.5 Å resolution. *Ultramicroscopy.* 19:147–178.

Henderson, R., J. M. Baldwin, T. A. Ceska, F. Zemlin, E. Beckmann, and K. H. Downing. 1990. Model for the structure of bacteriorhodopsin based on high-resolution electron cryo-microscopy. *J. Mol. Biol.* 213:899–929.

Herbette, L., P. DeFoor, S. Fleischer, D. Pascolini, A. Scarpa, and J. K. Blasie. 1985. The separate profile structures of the functional calcium pump protein and the phospholipid bilayer within isolated sarcoplasmic reticulum membranes determined by x-ray and neutron diffraction. *Biochim. Biophys. Acta.* 817:103–122.

Inesi, G. 1994. Teaching active transport at the turn of the twenty-first century: recent discoveries and conceptual changes. *Biophys. J.* 66: 554–560.

Inesi, G., L. Lu, M. E. Kirtley, and K. Takeyasu. 1994. Distinct structural identities of catalytic and Ca²⁺ binding domains in the sarcoplasmic reticulum ATPase. *Cell Physiol. Biochem.* 4:135–147.

Jap, B. K., P. J. Walian, and K. Gehring. 1991. Structural architecture of an outer membrane channel as determined by electron crystallography. *Nature.* 350:167–170.

Kühlbrandt, W., D. N. Wang, and Y. Fujiyoshi. 1994. Atomic model of plant light-harvesting complex by electron crystallography. *Nature.* 367:614–621.

Lacapere, J.-J., D. L. Stokes, and D. Chatenay. 1992. Atomic force microscopy of three-dimensional membrane protein crystals: Ca-ATPase of sarcoplasmic reticulum. *Biophys. J.* 63:303–308.

Lamvik, M. K., and S. Davilla. 1989. Calibration methods for quantitative image processing in electron microscopy. *J. Electron Microsc.* 11:97–101.

Leapman, R. D., J. Brink, and W. Chiu. 1993. Low-dose thickness measurement of glucose-embedded protein crystals by electron energy loss spectroscopy and STEM dark-field imaging. *Ultramicroscopy.* 52:157–166.

Lowry, O. H., N. J. Rosebrough, A. L. Farr, and R. J. Randall. 1951. Protein measurement with the folin phenol reagent. *J. Biol. Chem.* 193:25–275.

Misra, M., D. Taylor, T. Oliver, and K. Taylor. 1991. Effect of organic anions on the crystallization of the Ca^{2+}-ATPase or muscle sarcoplasmic reticulum. *Biochim. Biophys. Acta.* 1077:107–118.

Pederson, P. L., and E. Carafoli. 1987. Ion motive ATPases. 1. Ubiquity, properties, and significance to cell function. *TIBS.* 12:146–150.

Pikula, S., N. Mullner, L. Dux, and A. Martonosi. 1988. Stabilization and crystallization of Ca^{2+}-ATPase in detergent-solubilized sarcoplasmic reticulum. *J. Biol. Chem.* 263:5277–5286.

Stokes, D. L., and N. M. Green. 1990a. Structure of CaATPase: electron microscopy of frozen-hydrated crystals at 6 Å resolution in projection. *J. Mol. Biol.* 213:529–538.

Stokes, D. L., and N. M. Green. 1990b. Three-dimensional crystals of Ca-ATPase from sarcoplasmic reticulum: symmetry and molecular packing. *Biophys. J.* 57:1–14.

Stokes, D. L., W. R. Taylor, and N. M. Green. 1994. Structure, transmembrane topology and helix packing of P-type ion pumps. *FEBS Lett.* 346: 32–38.

Taylor, K. A., and S. Varga. 1994. Similarity of three-dimensional microcrystals of detergent-solubilized (Na^+,K^+)-ATPase from pig kidney and Ca^{2+}-ATPase from skeletal muscle sarcoplasmic reticulum. *J. Biol. Chem.* 269:10107–10111.

Taylor, K. A., L. Dux, and A. Martonosi. 1986. Three-dimensional reconstruction of negatively stained crystals of the Ca^{++}-ATPase from muscle sarcoplasmic reticulum. *J. Mol. Biol.* 187:417–427.

Taylor, K. A., N. Mullner, S. Pikula, L. Dux, C. Peracchia, S. Varga, and A. Martonosi. 1988. Electron microscope observations on Ca^{2+}-ATPase microcrystals in detergent-solubilized sarcoplasmic reticulum. *J. Biol. Chem.* 263:5287–5294.

Toyoshima, C. 1989. On the use of holey grids in electron crystallography. *Ultramicroscopy.* 30:439–444.

Toyoshima, C., H. Sasabe, and D. L. Stokes. 1993. Three-dimensional cryoelectron microscopy of the calcium ion pump in the sarcoplasmic reticulum membrane. *Nature.* 362:469–471.

Valpuesta, J. M., J. L. Carrascosa, and R. Henderson. 1994. Analysis of electron microscope images and electron diffraction patterns of thin crystals of Φ29 connector in ice. *J. Mol. Biol.* 240:281–287.

Varga, S., K. Taylor, and A. Martonosi. 1991. Effects of solutes on the formation of crystalline sheets of the Ca^{2+}-ATPase in detergent-solubilized sarcoplasmic reticulum. *Biochim. Biophys. Acta.* 1070: 374–386.

Wang, D. N., and W. Kühlbrandt. 1991. High-resolution electron crystallography of light-harvesting chlorophyll a/b-protein complex in three different media. *J. Mol. Biol.* 217:691–699.

Warren, G. B., P. A. Toon, N. J. M. Birdsall, A. G. Lee, and J. C. Metcalfe. 1974. Reconstitution of a calcium pump using defined membrane components. *Proc. Natl. Acad. Sci. USA.* 71:622–626.